



Article

New Remote Sensing Data on the Potential Presence of Permafrost in the Deosai Plateau in the Himalayan Portion of Pakistan

Maria Teresa Melis ^{*}, Francesco Gabriele Dessì and Marco Casu

Department of Chemical and Geological Sciences, University of Cagliari, Cittadella Universitaria-S.S. 554 Bivio per Sestu I, 09042 Monserrato, Italy; fdessi@unica.it (F.G.D.); rcooma@live.it (M.C.)

* Correspondence: titimelis@unica.it

Abstract: In this study, the presence of permafrost layer and its potential variation in the last three decades will be examined through the multitemporal analysis of satellite data in the area of the Deosai Plateau (Northern Pakistan). In the area, only global maps on the potential presence of permafrost layer are known. The results are based on the evaluation of variation of the number and water levels of the small lakes, and the changes of the extensions of the wetlands. The adopted methodology is based on the use of spectral indices and visual interpretation of a time-series data of Landsat images in the range 1990–2019, and on the processing of radar data from Sentinel 1 satellites, adopting new methods to extract the vertical displacement. The main findings are: (i) a high temporal dynamic of the number and surface areas of small lakes, and (ii) the evidence of a subduction in a wetland area (Black Hole), coherent with its extension, and suggesting the potential presence of a permafrost layer slowly degrading. This analysis can play a useful role on the management of the Deosai National Park (DNP), adopting careful measures for the human activities inside the park.

Keywords: Sentinel 1; Landsat; Deosai National Park; Himalaya range; permafrost; climate change; wetland



Citation: Melis, M.T.; Dessì, F.G.; Casu, M. New Remote Sensing Data on the Potential Presence of Permafrost in the Deosai Plateau in the Himalayan Portion of Pakistan. *Remote Sens.* **2023**, *15*, 1800. <https://doi.org/10.3390/rs15071800>

Academic Editor: Dehua Mao

Received: 5 February 2023

Revised: 7 March 2023

Accepted: 23 March 2023

Published: 28 March 2023



Copyright: © 2023 by the authors. Licensee MDPI, Basel, Switzerland. This article is an open access article distributed under the terms and conditions of the Creative Commons Attribution (CC BY) license (<https://creativecommons.org/licenses/by/4.0/>).

1. Introduction

The purpose of this study is to support the ecosystem management of the Deosai National Park (DNP) in northern Pakistan from an adaptation perspective to climate changes. With this aiming, a multitemporal analysis of satellite data has been applied to extract the morphological dynamics of lakes and wetlands, that, with the water courses, constitute in this area the favorable habitats of the flora and fauna species.

Indeed, DNP is part of the Deosai Plateau the second highest plateau in the world and highest on the Himalayas, with a valuable ecology and hosting the largest intact population of Himalayan Brown bear [1]. It is considered the core area for this species in the Hindu-Kush Karakorum Himalaya (HKH) region. Moreover, although the park is limited to 1600 sq. km, is home to about 24 mammalian species: predators other than Brown bear, like Snow leopard, Himalayan wolf and Tibetan Red fox and associated prey species mostly ungulates i.e., Himalayan ibex, Musk deer, and Golden marmot in or around DNP play a significant role in maintaining the ecological balance and health of the Park [1–4].

Due to these ecological reasons, and as part of the high mountains National Parks, the DNP is defined by the International Union for the Conservation of Nature (IUCN), as Category II type of Protected Areas: “large natural or near natural areas set aside to protect large-scale ecological processes, along with the complement of species and ecosystems characteristic of the area, which also provide a foundation for environmentally and culturally compatible spiritual, educational, scientific, educational, recreational and visitor opportunities” [4].

It is recognized that, in mountainous regions, where sometimes the fragile ecosystems have to coexist with the human activities, as pastoralism, the presence of protected areas involves the local communities in their preservation. For this reason, the ecosystem management has to be based on the knowledge of the specific environmental dynamics to propose the best executive actions. Therefore, the monitoring of land cover and morphological changes through remote sensing data can be a real support for the conservation of wildlife of this protected area, and for the understanding of the effects of human pressures [5].

This study is part of the activities carried out in the framework of the United Nation Development Program (UNDP) Project “Improvement of Central Karakoram National Park (CKNP) Management System as Model for Mountain Ecosystems in Northern Pakistan”, coordinated by the NGO (Non-Governmental Organization) EvK2CNR Pakistan [6]. In this project, a large number of data and local knowledge has been collected and organized in the Geographic Information System (GIS) environment to produce the thematic maps for the Management Plan of the DNP.

It is very important to underline that very few maps, reports and scientific literature have been produced to describe the environmental components of this region. Available papers focus mainly on the habitat of the Himalayan Brown bears and on the floristic biodiversity, but geological and geomorphological setting of this area is poorly known [7]. For these reasons, new information, based on the analysis of the existing elevation data (Global Digital Elevation Model), global thematic maps, and satellite images can give new suggestions on the environmental evolution of this area. Moreover, the existing new Land Cover Map of DNP, based on ESA Sentinel 2 imagery and produced in the UNDP Project by the authors has been used to use the information on the distribution and types of lands and vegetation features. This map was validated during a field survey [6].

With the aim to identify the environmental changes occurred in the last decades on the surface of the plateau, and probably related to climate change effects, a diachronic analysis of remote sensing data has been done. This analysis focused on the mapping and temporal dynamics of wetlands and water bodies, as main habitats of the plateau.

The multitemporal analysis, based on the available data of Landsat satellites and ESA Sentinel 1 and 2, reveals new indications on the recent environmental dynamics referred to water resources. Analyzing the satellite data, a large number of small lakes has been recognized. Their number and extension have been measured from the multitemporal satellite data, and the proposed interpretation of the observed changes is here referred to the potential presence of a permafrost layer and its degradation due to climate warming [8]. The behavior of the effects of the permafrost degradation, as suggested in other geographical areas, can consist of disappears or changes of the boundaries of periglacial lakes, or transition from large water basins to small new ponds.

Moreover, the subsidence rate calculated from interferometric data can support the hypothesis on the presence of a permafrost layer, potentially estimated at global scale [9].

As discussed in literature, the permafrost status can be monitored using radar data to extract the terrain deformation due to thawing subsidence, collapses and changes of the water circulation [10–14]. With this study we will use an indirect approach that can contribute to indicate the existence of potential permafrost through remote identification and mapping of surface landforms, as suggested for local areas where the recognition of the landforms can be done [15].

2. Study Area

DNP is part of the Deosai Plateau in the Northern Areas of Pakistan (Figure 1).

The Park, covering an area of around 1600 sq km, has an altitude ranging from 3500 to 5200 m a.s.l. The central part of the Park is relatively flat and gentle (Figure 2) with lower elevation of 4000 m. Almost 63% of the area has an elevation range from 4000 to 4500 m, and 22% of the area is above 4500 m making the Deosai Plains highest plateau in the world after Changtang Tibetan Plateau.

During the summer season a very large number of rivers flow. Indeed, the plateau is characterized by the presence of areas of wetlands and numerous small lakes. Their origin is due to snow and ice melting from the surrounding steep mountains. Moreover, in the flat areas the presence of depressions and circular small lakes can support the presence of a periglacial landscape [16–18].

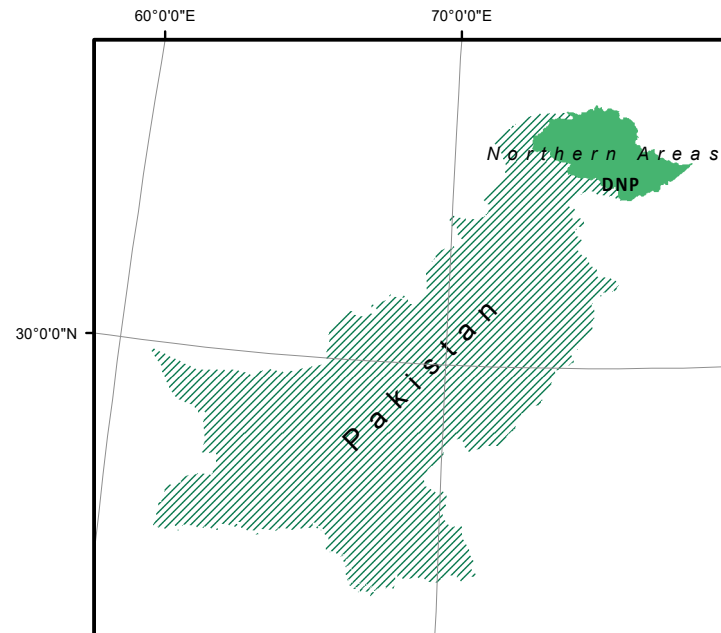


Figure 1. Localization of the Deosai National Park (DNP) in the Deosai Plateau in the Northern Areas region of Pakistan.

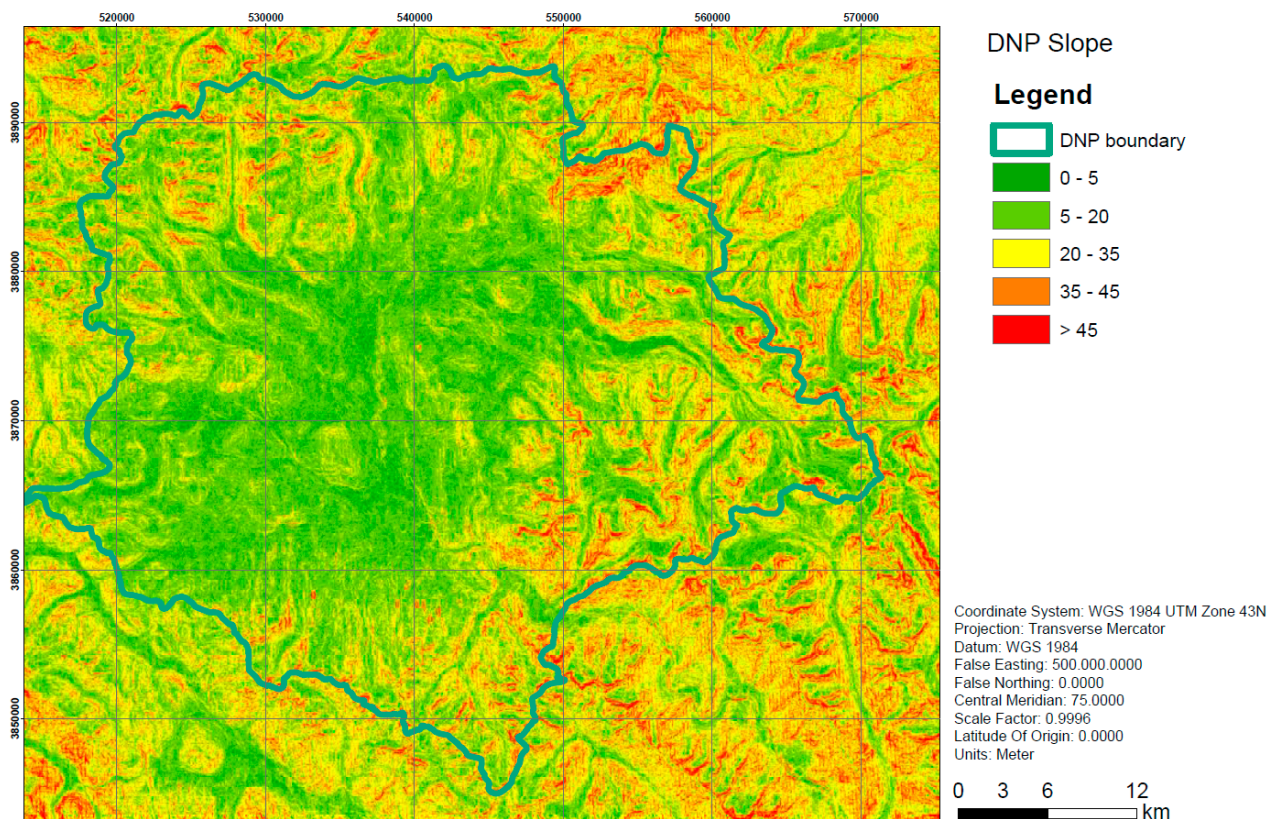


Figure 2. The slope map of the DNP (data are expressed in degrees).

The plateau is localized at the convergence of the mountain ranges of Himalayan and Karakorum-Pamir highlands, and was affected by the climatic variations of the late Holocene in its geomorphological evolution [19,20]. The geological evolution of the plateau is linked to the plutonic events of the Ladakh igneous belt with a cover sequence of different volcanic rocks. Quaternary glacio-fluvial and alluvial deposits cover the plateau and sign the geomorphological dynamics [7].

As displayed in the Land Cover map in Figure 3, the grassland and shrublands are predominant on the plateau. They constitute the habitats of the Himalayan Brown bears, as signed in the map. As cleared in the graphic in Figure 3, the class defined as “Regularly flooded shrub/herbaceous cover” has an important role in the ecosystem of the DNP, with a surface of around 11% of the total. These wetlands and the small lakes are supplied by the water flowing from the very few and small melting glaciers, and for some of them can be proposed the underground source, as the presence of a permafrost layer.

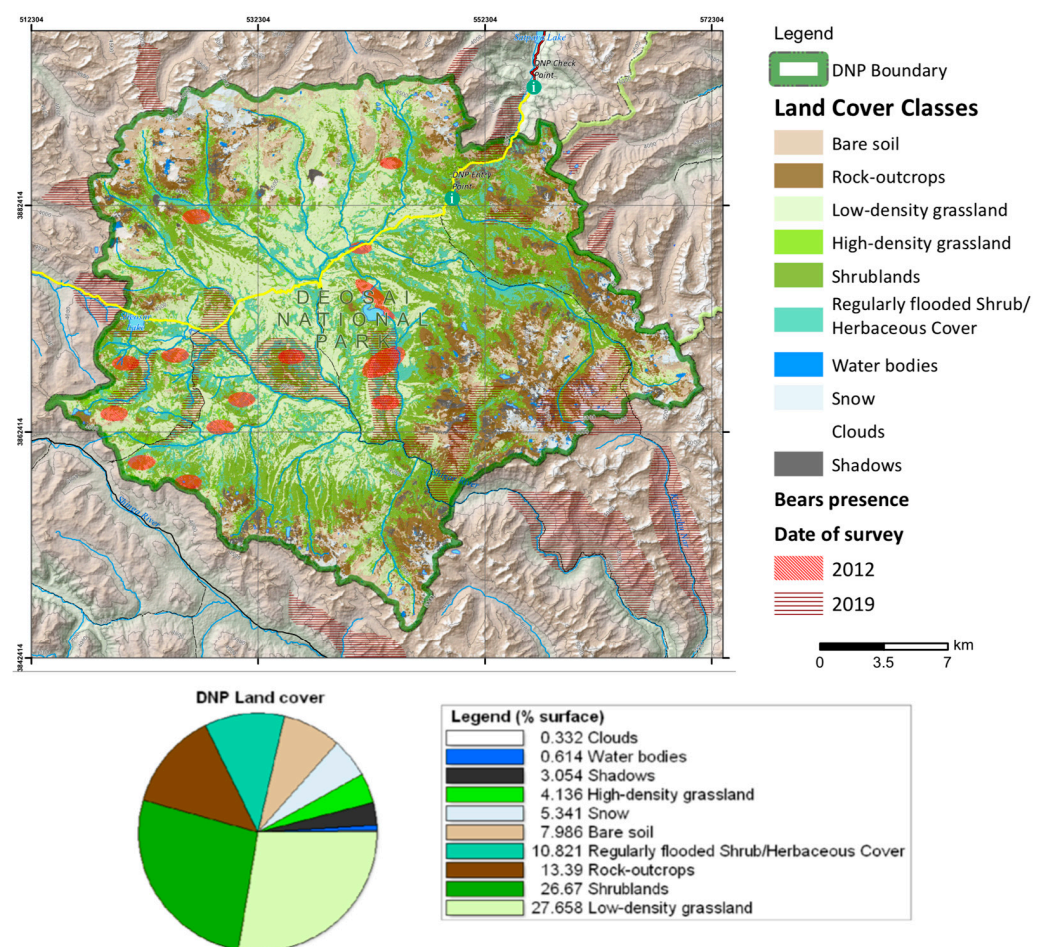


Figure 3. The Land Cover map of the DNP.

The climate of the plateau is characterized by temperature and precipitation highly seasonal with extreme environmental conditions. The mean daily temperatures range from $-20\text{ }^{\circ}\text{C}$ to $12\text{ }^{\circ}\text{C}$, and annual precipitation varying between 510 and 750 mm, mostly as snow [1,2].

In this study, the known permafrost existence on Deosai plateau has been extracted from the available global maps of permafrost probability [9,15]. Very few and sparse direct observations of permafrost in the HKH mountains are available [21]. The resulting distribution is displayed in Figure 4. Along the border of the plateau, where the high elevations and steep ridges constitute the natural watershed, both maps highlight the presence of a continuous and discontinuous permafrost layer (high probability). At the

lower elevation and in the flatter areas, where the landscape appears with depressed areas (wetlands in the summer season), and small lakes, its occurrence is considered isolated or sporadic (lower probability).

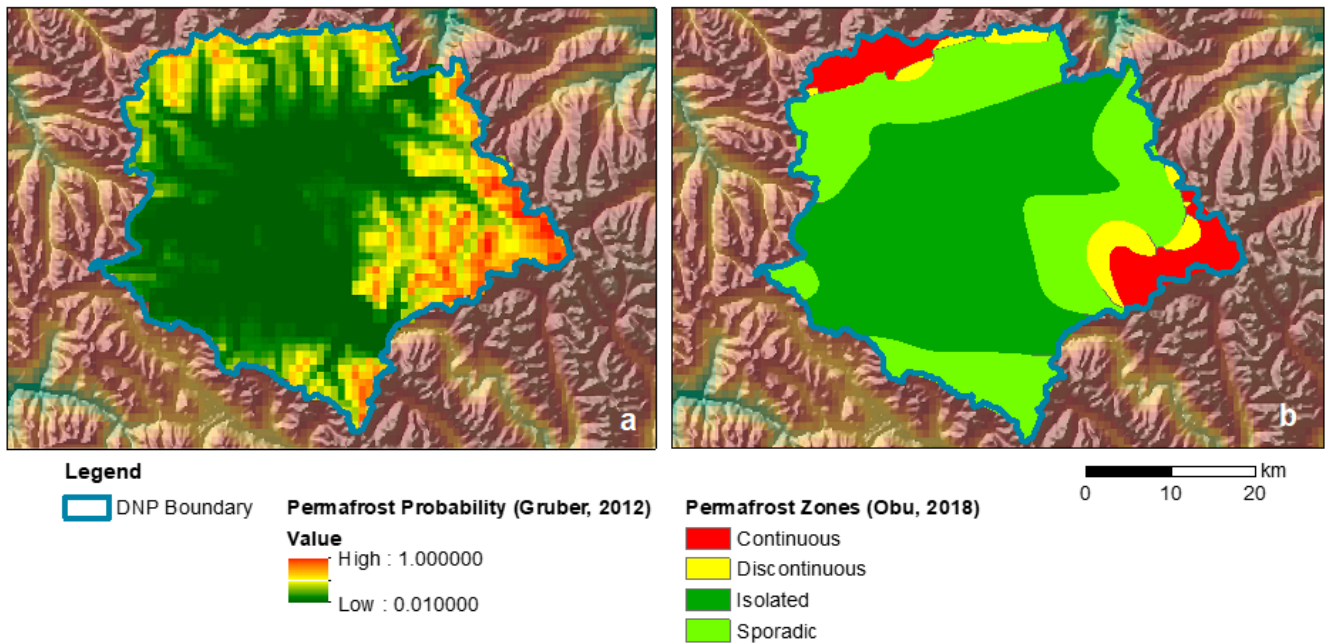


Figure 4. Maps of the permafrost probability (a), and permafrost zones (b), adapted the freely available global models [9,15].

3. Materials and Methods

3.1. Satellite Imagery

In this study, two sets of satellite data have been used (Tables 1 and 2):

- Time-series of Landsat data
- ESA Sentinel 1

Table 1. Landsat images acquired in this study.

Satellite	Path	Acquisition Date
Landsat 4-5	149-36	7 August 1990
Landsat 4-5	149-36	3 September 1994
Landsat 4-5	149-36	10 August 1997
Landsat 4-5	149-36	30 September 1998
Landsat 4-5	149-36	16 August 1999
Landsat 7	149-36	26 August 2000
Landsat 7	149-36	30 September 2001
Landsat 4-5	149-36	25 September 2008
Landsat 4-5	149-36	27 August 2009
Landsat 8	149-36	7 September 2013
Landsat 8	149-36	17 August 2017
Landsat 8	149-36	21 September 2018
Landsat 8	149-36	24 September 2019

Table 2. List of the Sentinel 1 data acquired in this study.

Orbit	Number of Images	Master Image Date	Time Reference	
			Start	End
Ascending	26	18 August 2019	15 July 2014	31 August 2022
Descending	16	29 August 2017		

The optical Landsat images were chosen between the summer acquisition on August and September, considering the glaciers and waterbodies melting, which is reflected in the maximum water level.

Moreover, the ESA Sentinel 2 imagery (acquisition date 20180806) used for the extraction of the Land Cover map, realized by the authors and already available for this study, has been acquired.

3.2. Permafrost Maps

Two available Global permafrost maps have been collected (Figure 4):

- The Global Permafrost Zonation Index Map: The Global Permafrost Zonation Index Map has a resolution of 30 arc-seconds (about 1 km) and is available for all land areas except for Antarctica. It is available digitally for Google Earth, as a Web Mapping Service and, as raw data [9].
- The Permafrost Zonation: The product, at 1 km spatial resolution, provides the Permafrost probability (fraction values from 0 to 1). Each grid cell is classified as continuous, discontinuous and sporadic permafrost on the basis of its permafrost probability. It is provided also as classified shapefile [15].

3.3. Lakes Extraction from Satellite Data

The application of atmospheric correction and transformation in reflectance values have been applied to each image of every year. Then, the recognition of the lakes has been carried out.

The cloud and snow masking have been calculated, and the spectral indices NDWI (Green-NIR/Green + NIR) and NDVI (NIR-Red/NIR + Red) were applied to each image.

The thresholds to extract the waterbodies from these indices were not uniform, due to the presence of suspended solid or organic matter in the water [22]. As well-known, small lakes in mountains areas can be affected by different uncertainty, and the application of these indices has to be supported by a visual inspection by an expert. Comparing the composite RGB images with the NDWI and NDVI indices for each year, the final lakes boundaries were obtained. This visual interpretation improved the classification based on the indices alone, and guaranteed the potential mis-interpretation of water and shadows.

3.4. Wetlands Extraction

In this study, the wetlands were extracted each ten years, starting from 1990. On the Landsat images acquired on 1990, 2000, 2009 and 2019, the wetlands have been recognized using the NDVI and the total surface of each image has been calculated. The wetlands were extracted applying the spectral index that enhance the pixel with a high reflectance of the vegetation associated to the wetland. For this reason, the best period is the summer month of August when the maximum phenological state of vegetation can be observed.

3.5. Terrain Displacement

The technical characteristics and the freely available use of the Sentinel-1 constellation can provide new and powerful tools for monitoring purposes. Indeed, this two-satellite system offers a revisit time between 6 (at the equator) and 24 days (at higher latitude). Moreover, it is equipped with an orbital tube diameter of 300 m, providing less noisy interferograms [23].

SAR interferometry has become a good technique to investigate land deformation phenomena with the possibility to measure ground displacements with a very high level of accuracy (1–2 mm/year), oriented along the Line Of Sight (LOS) directions. During last years, the temporal and spatial resolution improved with a good benefit in terms of applications to observations to earth surface dynamics [24–27].

In the differential SAR Interferometry (InSAR) methodologies, interferogram's stacking has a primary key role in the processing chain. In this work, we used the Persistent Scatterer Interferometry (PSI) technique in order to get the velocity of fixed and very high

coherent scatterers through images acquisitions of Sentinel-1A satellite by ESA [28–30]. Sentinel data has given totally free of charge with the possibility to process SAR datasets by means of freely accessible software and tools: ESA has released the (Sentinel Application Platform (SNAP) software with a good network of developers and supporting team. The relative movement of persistent scatterers can be calculated from the interferograms obtained by SNAP and ingesting them in the Stanford Method for Persistent Scatterers (StaMPS) free tool, as stated in some studies where the PSI method has been carried out by ascending and descending orbits combination [31–34].

The processing workflow is displayed in Figure 5.

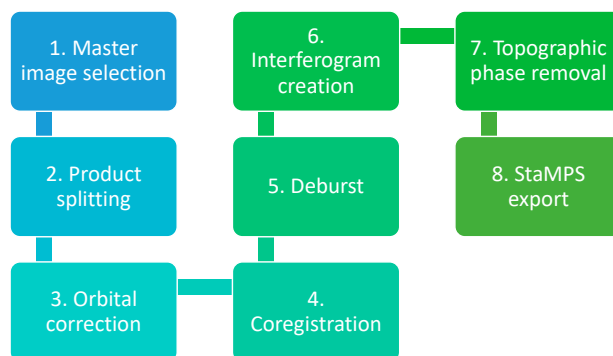


Figure 5. Workflow of the InSAR processing.

Therefore, the next steps were followed: (1) Using of the optimal InSAR master selection tool by SNAP; (2) For all of the data, the same sub-swath and bursts needs to be selected, in order to get the co-registration between images; (3) The Sentinel orbit files provided by ESA are applied to the complete dataset; (4) The coregistration is performed exploiting the Back Geocoding operator; (5) In the deburst step, adjacent bursts are merged together in the azimuth direction according to their zero-Doppler times; (6) Calculation of the complex interferograms; (7) The topographic phase is computed and subtracted from the interferograms with the SRTM 3 arcseconds DEM downloaded by the software automatically; (8) In the last step, it is necessary to prepare the folder structure of dataset as required by StaMPS, starting from the previous products.

The processing parameters for PSI analysis by StaMPS has been set using the available `mt_prep_snap` script. Parameters like the amplitude dispersion (D_a) and the number of overlapping pixels in the azimuth (n_a) and range (n_r) are left as default ($D_a = 0.4$; $n_r = 50$; $n_a = 200$). The stack of interferograms is processed using MATLAB procedures implemented in StaMPS with the combination of the tropospheric corrections provided by TRAIN module [35]. At the end of StaMPS processing, the TRAIN linear phase-based correction is applied (Figure 6).

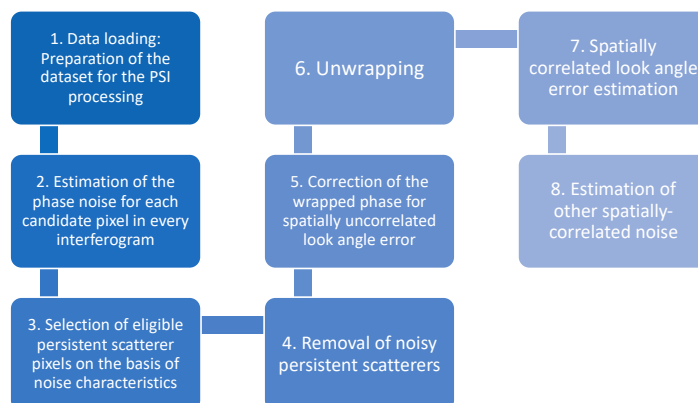


Figure 6. Workflow of TRAIN processing.

The velocity values that it is possible to calculate are relative to the mean velocity of the whole image. At this step it is possible to select a reference site and introduce an average velocity for it (typically an accurate GPS measurement). In this way, the whole dataset can be referred to this reference velocity. In our case this kind of measure is not available. Anyway, it is possible to select a reference area where no change is expected.

For our study area we select a circular reference area centered in coordinates 75.4627 E and 35.0586 N (degrees) with a radius of 10 km.

At the end of the processing a vector shapefile was exported in order to perform further analysis in GIS environment. In the attribute table, we exported LOS velocities for each persistent scatterer. In particular a single shapefile related to ascending orbit and another related to descending orbit was created.

In order to get the vertical displacements, it is necessary to apply a decomposition procedure, related to both ascending and descending LOS velocities calculation and linked to acquisition geometry. Results of both geometries were then combined to compute the actual vertical motion component. For each point it is necessary to consider a couple (Ascending and Descending) of values.

In order to avoid interpolation between measurement, with an increasing of uncertainties by introducing a significant smoothing of the initial PSI measurements, a vector-based approach has been managed accordingly with [36]. The analysis concerned the identification for each point in one geometry of its closest in the second geometry by means of nearest neighbour vector analysis. In this way the calculation involved only one nearest neighbour point between the two geometries and not an average of several closest points.

Since PS points are not regularly distributed in space, the distances from their closest neighbour in the opposite geometry is changing, in our case with an average of around 30 m. In order to elude the connection of very far points, since they might not be sharing common behavior in terms of ground displacement, a maximum search radius was introduced as a limitation, restricting the analysis within distances shorter than 100 m. To this end, the distance constraint was arbitrary defined as being three times higher than the average distance between PS points. Points failed to meet the above condition were rejected from further analysis.

4. Results

4.1. Optical Data

The extraction of lakes from the time-series analysis of Landsat imagery returned the data in Table 3. In Table 4 the wetland surfaces of the study area are given, referred to the four Landsat acquisitions.

Table 3. The table shows the surfaces (sq. km) and the number of lakes extracted from each image.

Acquisition Year	Acquisition Month	Total Surface (sq. km)	Total Number of Lakes
1990	August	11.4	203
1994	September	11.1	220
1997	August	11.3	240
1998	September	10.7	186
1999	August	8.2	164
2000	August	10.1	221
2001	September	11.4	227
2008	September	10.3	198
2009	August	10.6	253
2013	September	10.9	256
2017	August	8.7	216
2018	September	10.1	232
2019	September	9.9	217

These results are displayed in Figure 7. Four maps, referred to the four years 1990, 1000, 2009 and 2018 have been created to show the geographic distribution of the lakes and

wetlands in the different time. It can be seen that 66 lakes can be considered permanent in the range of the considered forty years, as they were present in each of the 13 images from 1990 to 2019. Moreover, in the maps, the number of lakes in the year of reference are displayed: 203 in 1990, 139 in 2000, 190 in 2009, and 175 in 2018.

Table 4. The table shows the total surfaces covered by wetlands (sq. km) extracted from each image.

Date of Acquisition	Wetlands Surface (sq. km)
1990	92.7
2000	77.9
2009	13.9
2018	175.5

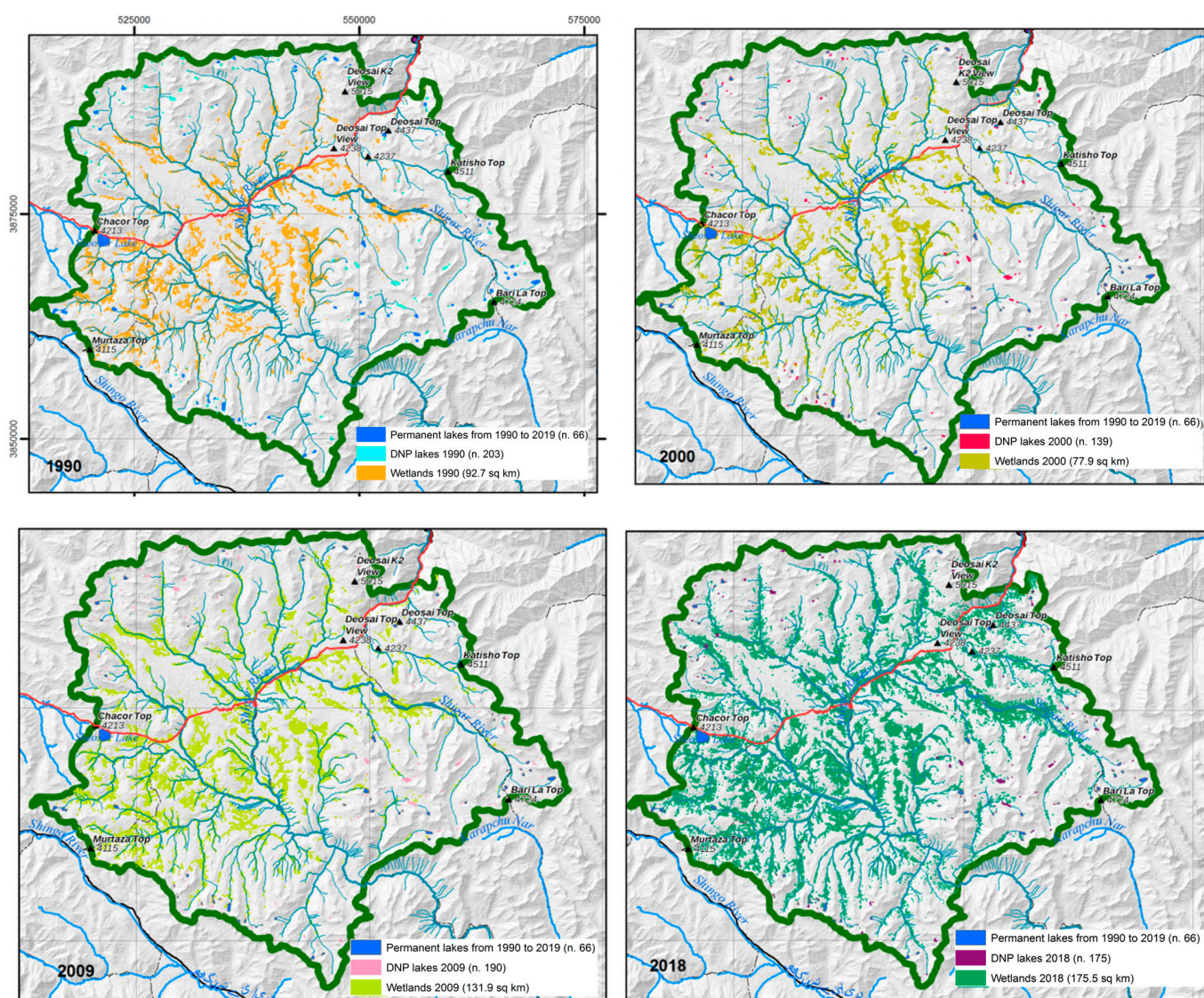


Figure 7. Diachronic maps of the distribution of lakes and wetlands in DNP. The coordinates are expressed in meters, as in Figure 2.

The number and surfaces of the lakes have been analysed in the GIS environment extracting the following information:

- 66 lakes are permanent from 1990;
- The number and the total surface of the small lakes show a gentle decrease from 1990 toward 2019 (Figure 8a);

- The surface of the wetlands shows a clear increasing in the considered interval (Figure 8b).

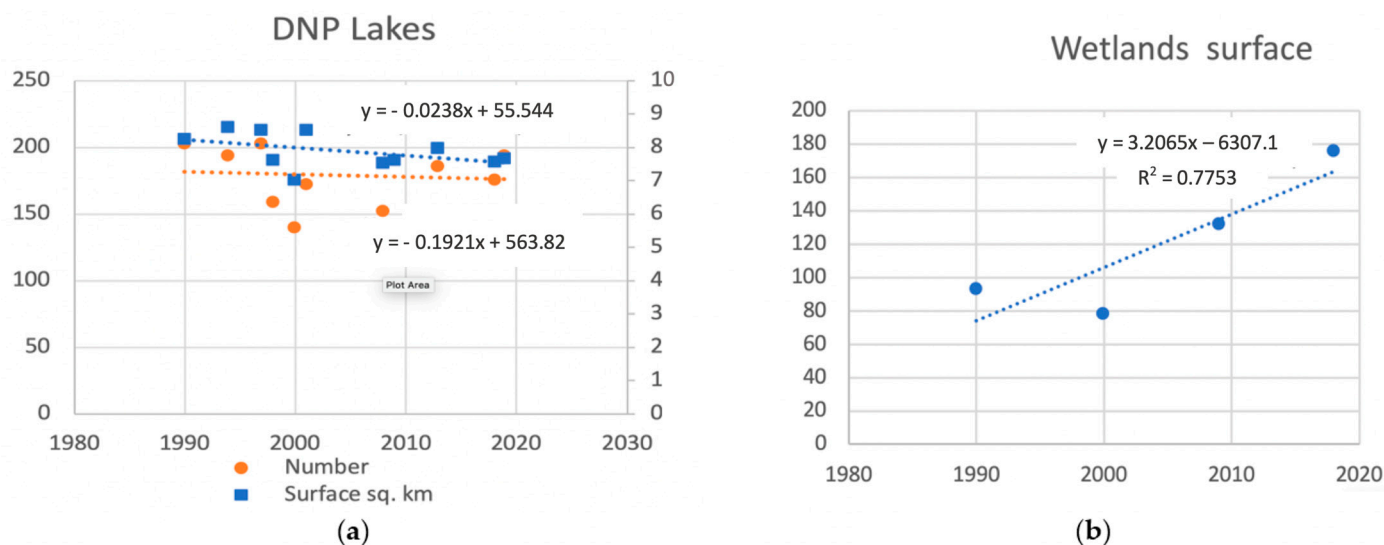


Figure 8. (a) Distribution of the number and surfaces of the lakes extracted from the Landsat series. (b) Surfaces of the wetlands obtained from the four Landsat images in Table 4.

4.2. SAR Data

The interferometric processing of Sentinel-1 images acquired from both ascending and descending orbits produced first of all two georeferenced LOS velocity (mm/year) maps of the study area. To exclude scatterers with low temporal coherence we ignored pixels with amplitude dispersion $Da < 0.4$. Accordingly, displacement rates have been computed by taking in account a reference area that is supposed to be stable.

The time series with the deformation data, related to each observation, is available for individually point. These series can show linear trends with a dispersion of few millimeters. Through the decomposition of LOS velocities, the vertical displacement has been computed and a new geocoded file has been generated. This new velocity map shows deformation phenomena related to each geographic domain. Vertical velocities have been statistically analyzed, and the results are given on Table 5.

Table 5. Statistical values calculated for Vertical Velocities points in the whole study area. Max and Min values are the Maximum (positive) and Minimum (negative) velocities with their relative accuracy. The Standard dev. column is the population standard deviation of the data. The median is the value in the middle of the data set. Q1 and Q3 are respectively the lower and the upper quartiles and the IQR is the Inter Quartile Range, a measure of statistical dispersion.

Max Value (mm/yr)	Min Value (mm/yr)	Standard Dev.	Median	Q1	Q3	IQR
5.207 ± 0.1	-6.235 ± 0.1	0.749	0.129	-0.317	0.524	0.841

Velocities measurement roughly spans from values between -6 mm/yr and $+5$ mm/yr with an Interquartile Range (IQR) of 0.841.

Positive values have to be interpreted as a relative uplift of the persistent scattered and negative values have to be associated to a relative subsidence motion.

These results have been mapped in raster format applying the Inverse Distance Weighted (IDW) interpolation (12 points and 2 as power).

Starting from the optical results, the interferometric study has been focused on a specific area, where a morphological depression, known as Black Hole, can be considered a peatland, surrounded by a large wetland. In this area, the increasing values of inundated area along the time series have been detected and the values of subsidence from interferometric analysis are clear (Figure 9).

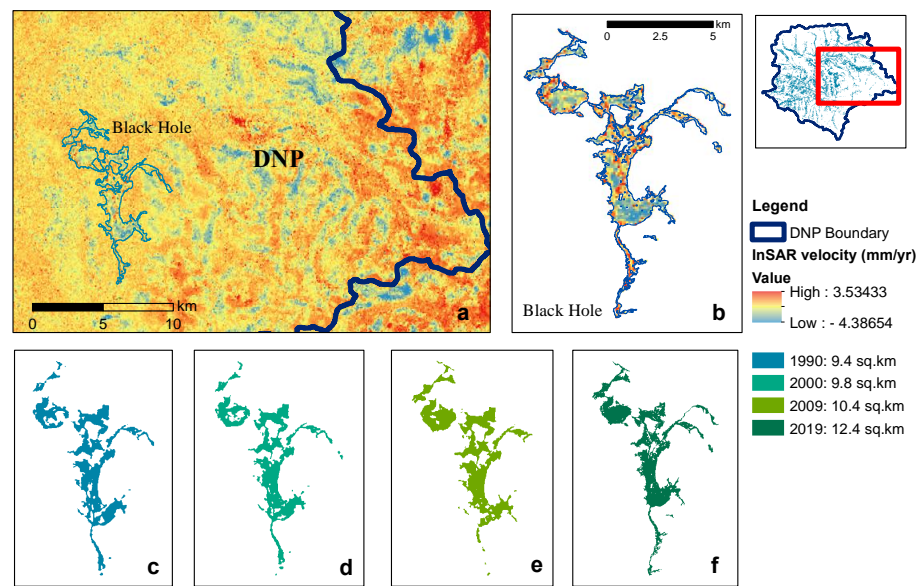


Figure 9. (a) Map of the Vertical velocities values, and in (b) on the Black Hole; (c–f) extension of the wetland from optical data in the range 1990–2019. The red box of the high-right map of the DNP represents the area in (a).

5. Discussion

The trend of the changes of the total surfaces and number of lakes from 1990 to 2019, in Figure 8a, shows that there is a general tendency of low decreasing of the total number and of the total surfaces during the considered time. Furthermore, from the analysis of the single number and localization of lakes in each year seems that only 66 lakes are permanent during this period, and for each analyzed year, new lakes appear and disappear. This dynamic can confirm the presence of an important sub-surficial hydrological activity. This general low-decreasing trend of the number and surfaces of the small lakes, related to the geomorphological/hydrological dynamics of the plateau can be considered in line with the dynamics of periglacial lakes in other regions [37].

To understand better the seasonal dynamics of these small lakes, the results of the analysis has been filtered by the months August and September. Some interesting results occur, that can be interpreted as changes of the permafrost setting (Figure 10).

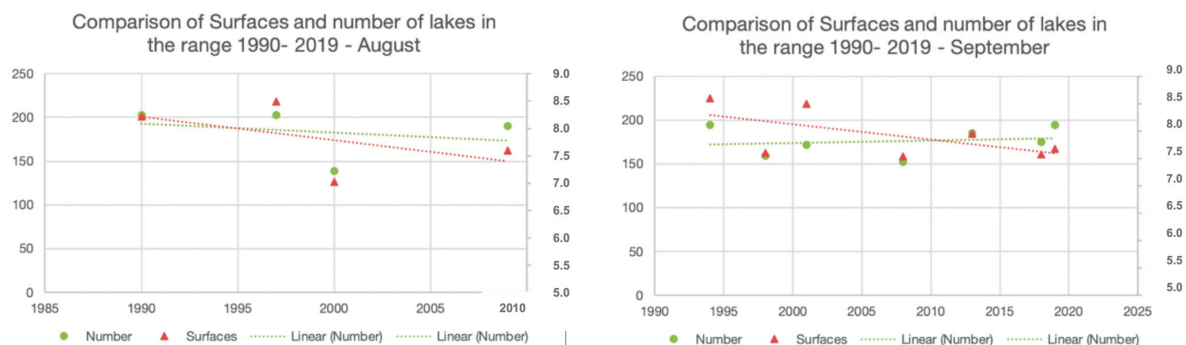


Figure 10. The graphs show the total surfaces (sq. km) and the number of lakes extracted from each image of August (left) and September (right).

It can be observed that: (i) the surface and the number of lakes in August have a gentle negative trend; (ii) instead in September, while surfaces show a decrease, the number of lakes have a weak positive trend. As discussed in [38], in the areas of discontinuous permafrost, during the first phase, the water drainage due to the thawing of the permafrost layer modifies the waterbody until it disappears (surfaces and number decreasing). In the

second phase the remaining lakes decrease in surface area. In this study, the behavior of the lakes seems to confirm this model.

Regarding the analysis of the wetlands, starting from the increasing of their total surface area, the results in the area of the Black Hole, show a similar trend over time, comparing with the total wetlands (Figure 11). Moreover, the vertical velocities values, measured from the interferometric analysis, confirm a subsidence of this area comparing with the surroundings. This process, with the lateral expansion of the depression is explained in [39], where this modification derived from climate warming can be considered the first phase of permafrost degradation. This step can be followed by the complete drainage of the depression. Furthermore, in the depression of the Black Hole, when there is no water, clear drainage pattern and polygonal patterned ground soil are visible, suggesting the presence of the permafrost layer.

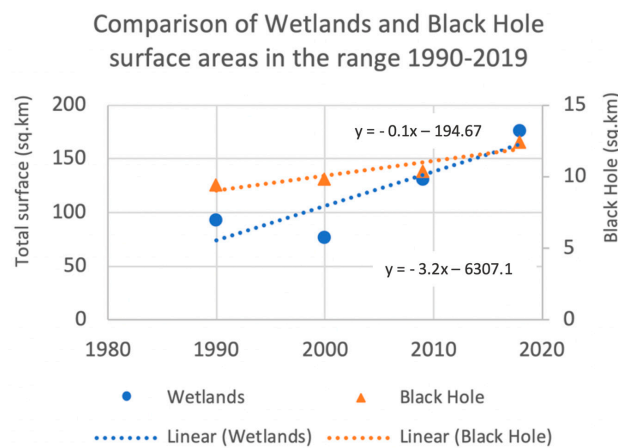


Figure 11. Trends of the changes of total surfaces of wetlands and of Black Hole over time.

Moreover, the dynamics of small lakes in the areas where permafrost layer are known is considered faster than in the wetlands, and in particular in the peatlands, where the permafrost degradation can be protected by the organic layer [39]. This observation can justify the trends that we observed, confirming the presence of permafrost layers in DNP, which were proposed as isolated zone ([15] and with low probability [9] (Figure 12).

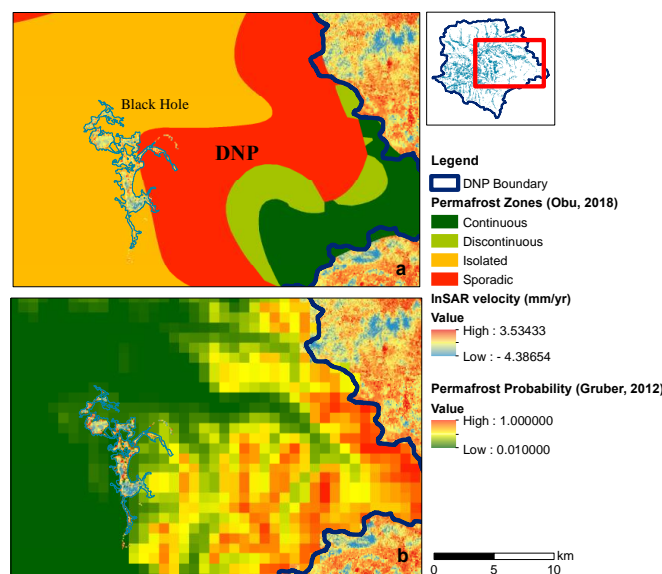


Figure 12. Maps of the study area of Black Hole with: (a) the permafrost zoning [15] and (b) the permafrost probability index by Gruber, 2012 [9]. The red box of the high-right map of the DNP represents the area in (a,b).

6. Conclusions

This study can add some new information on the potential permafrost presence in the mountainous of HKH area where the few studies regarding permafrost are mainly focused on the rock glaciers environment [21,40–42].

The use of remote sensing data, and the integration of results from different sensors, as expected, can be considered crucial for the acquisition of new information and extend the data collected in the field mainly in remote areas, where the surveys are limited [43].

The use of interferometric data can improve the results of optical data, allowing to understand the geomorphologies dynamics of the depressions with a third dimension, as the vertical velocity values.

These first results are coherent with the outcomes of other studies in different zones of the earth with a permafrost landscape. Changes in the characteristics of hydrological discharge and in soil moisture can be interpreted in many areas of the earth as hydrological reflections of the changes in permafrost and active layer thickness. Changes in permafrost and active layer depth directly affect the subsurface water storage and as such can be expected to also affect river discharge.

As discussed, lakes, ponds, and wetlands appear with different dynamics, growing in some areas, shrinking in others, and changing distribution across the plateau. These changes can be interpreted as result from a system-wide response to changing climate arising from a region-wide warming, subsequent glaciers melting and thawing of permafrost.

The results obtained in Deosai demonstrate that landscapes may be particularly sensitive to climate change and capable of rapid geomorphic responses to perturbations.

It is important to underline that it is the first time that an analysis like this was done on the Deosai plateau. Moreover, these results can be considered preliminary and integration of climate records are required to validate the evidences from remote sensing data.

Moreover, the presence and characterization of permafrost layers can be confirmed by the evaluation of the ground ice content only with the essential acquisition of the geologic and geomorphological data in the field.

Furthermore, it would be desirable that, if the permafrost layer is recognized, a permanent observing of its status with the installation of weather stations and monitoring boreholes is planned to assure the conservation of this so fragile and so rich in biodiversity ecosystem.

Author Contributions: Conceptualization, M.T.M. and F.G.D.; methodology, M.T.M. and F.G.D.; formal analysis, M.T.M., F.G.D. and M.C.; data curation, M.T.M., F.G.D. and M.C.; writing—original draft preparation, M.T.M. and F.G.D.; review and editing, M.T.M.; supervision, M.T.M.; project administration, M.T.M.; funding acquisition, M.T.M. All authors have read and agreed to the published version of the manuscript.

Funding: This research was funded by EvK2-CNR Pakistan Association in the framework of the agreement between the Department of Chemical and Geological Sciences of the University of Cagliari, Italy, and the EvK2-CNR Pakistan Association (UNICA prot. N. 0038701- 05/02/2019). This study is part of the United Nation Development Program (UNDP) Project Improvement of Central Karakoram National Park (CKNP) Management System as Model for Mountain Ecosystems in Northern Pakistan”, coordinated by the NGO (Non-Governmental Organization) EvK2CNR Pakistan.

Acknowledgments: The authors acknowledge the technical support of EvK2CNR Pakistan, and in particular Muhammad Aurang Zaib, Riaz Ul Hassan, Arif Hussain and Maurizio Gallo for the field activities and the sharing of local knowledge and useful discussions.

Conflicts of Interest: The authors declare no conflict of interest. The funders had no role in the design of the study; in the collection, analyses, or interpretation of data; in the writing of the manuscript, or in the decision to publish the results.

References

- Nawaz, M.A.; Swenson, J.E.; Zakaria, V. Pragmatic Management Increases a Flagship Species, the Himalayan Brown Bears, in Pakistan's Deosai National Park. *Biol. Conserv.* **2008**, *141*, 2230–2241. [[CrossRef](#)]
- Nawaz, M.A.; Martin, J.; Swenson, J.E. Identifying Key Habitats to Conserve the Threatened Brown Bear in the Himalaya. *Biol. Conserv.* **2014**, *170*, 198–206. [[CrossRef](#)]
- Dar, S.A.; Singh, S.K.; Wan, H.Y.; Kumar, V.; Cushman, S.A.; Sathyakumar, S. Projected Climate Change Threatens Himalayan Brown Bear Habitat More than Human Land Use. *Anim. Conserv.* **2021**, *24*, 659–676. [[CrossRef](#)]
- Baig, S.U.; Malik, A.J.; Khan, H. Wildlife Habitat-Suitability Analysis for High Mountain National Parks in the Hindu Kush, Karakoram and Himalayan Region of Northern Pakistan. *Model. Earth Syst. Environ.* **2022**, *8*, 3941–3956. [[CrossRef](#)]
- Duan, P.; Wang, Y.; Yin, P. Remote Sensing Applications in Monitoring of Protected Areas: A Bibliometric Analysis. *Remote Sens.* **2020**, *12*, 772. [[CrossRef](#)]
- Melis, M.T.; Dessi, F.; Loddo, P.; Maccioni, A.; Gallo, M.; Ul Hassan, R.; Aurang Zaib, M. ESA Sentinel 2 Imagery and GBGEOApp: Integrated Tools for the Deosai National Park Management Plan. *Int. Arch. Photogramm. Remote Sens. Spat. Inf. Sci.* **2020**, *43*, 145–151. [[CrossRef](#)]
- Jadoon, U.K.; Ding, L.; Baral, U.; Qasim, M. Early Cretaceous to Eocene Magmatic Records in Ladakh Arc: Constraints from U–Pb Ages of Deosai Volcanics, Northern Pakistan. *Geol. J.* **2020**, *55*, 5384–5397. [[CrossRef](#)]
- Hussain, N.; Ali, S.; Hussain, A.; Ali, S.; Khan, S.W.; Raza, G.; Abbas, Q.; Hussain, I.; Hussain, M. Climate Change Variability Trends and Implications for Freshwater Resources in Pakistan's Eastern Hindu Kush Region. *Pol. J. Environ. Stud.* **2018**, *27*, 665–673. [[CrossRef](#)]
- Gruber, S. Derivation and Analysis of a High-Resolution Estimate of Global Permafrost Zonation. *Cryosphere* **2012**, *6*, 221–233. [[CrossRef](#)]
- Zou, L.; Wang, C.; Tang, Y.; Zhang, B.; Zhang, H.; Dong, L. Interferometric SAR Observation of Permafrost Status in the Northern Qinghai-Tibet Plateau by ALOS, ALOS-2 and Sentinel-1 between 2007 and 2021. *Remote Sens.* **2022**, *14*, 1870. [[CrossRef](#)]
- Wang, S.; Xu, B.; Shan, W.; Shi, J.; Li, Z.; Feng, G. Monitoring the Degradation of Island Permafrost Using Time-Series InSAR Technique: A Case Study of Heihe, China. *Sensors* **2019**, *19*, 1364. [[CrossRef](#)]
- Chen, J.; Wu, T.; Zou, D.; Liu, L.; Wu, X.; Gong, W.; Zhu, X.; Li, R.; Hao, J.; Hu, G.; et al. Magnitudes and Patterns of Large-Scale Permafrost Ground Deformation Revealed by Sentinel-1 InSAR on the Central Qinghai-Tibet Plateau. *Remote Sens. Environ.* **2022**, *268*, 112778. [[CrossRef](#)]
- Short, N.; Brisco, B.; Couture, N.; Pollard, W.; Murnaghan, K.; Budkewitsch, P. A Comparison of TerraSAR-X, RADARSAT-2 and ALOS-PALSAR Interferometry for Monitoring Permafrost Environments, Case Study from Herschel Island, Canada. *Remote Sens. Environ.* **2011**, *115*, 3491–3506. [[CrossRef](#)]
- Rudy, A.C.A.; Lamoureux, S.F.; Treitz, P.; Short, N.; Brisco, B. Seasonal and Multi-Year Surface Displacements Measured by DInSAR in a High Arctic Permafrost Environment. *Int. J. Appl. Earth Obs. Geoinf.* **2018**, *64*, 51–61. [[CrossRef](#)]
- Obu, J.; Westermann, S.; Kääb, A.; Bartsch, A. Ground Temperature Map, 2000–2016, Northern Hemisphere Permafrost. *Alfred Wegener Inst. Helmholtz Cent. Polar Mar. Res. Bremerhav.* **2018**. [[CrossRef](#)]
- Brown, J.; Romanovsky, V.E. Report from the International Permafrost Association: State of Permafrost in the First Decade of the 21st Century. *Permafrost Periglacial Process.* **2008**, *19*, 255–260. [[CrossRef](#)]
- Karlsson, J.M.; Lyon, S.W.; Destouni, G. Thermokarst Lake, Hydrological Flow and Water Balance Indicators of Permafrost Change in Western Siberia. *J. Hydrol.* **2012**, *464–465*, 459–466. [[CrossRef](#)]
- Yoshikawa, K.; Hinzman, L.D. Shrinking Thermokarst Ponds and Groundwater Dynamics in Discontinuous Permafrost near Council, Alaska. *Permafrost Periglacial Process.* **2003**, *14*, 151–160. [[CrossRef](#)]
- Meiners, S. The Glacial History of Landscape in the Batura Muztagh, NW Karakoram. *GeoJournal* **2005**, *63*, 49–90. [[CrossRef](#)]
- Iturrizaga, L. The Valley of Shimshal—A Geographical Portrait of a Remote High Mountain Settlement and Its Pastures with Reference to Environmental Habitat Conditions in the North-West Karakoram (Pakistan). *GeoJournal* **1997**, *42*, 303–328. [[CrossRef](#)]
- Gruber, S.; Fleiner, R.; Guegan, E.; Panday, P.; Schmid, M.-O.; Stumm, D.; Wester, P.; Zhang, Y.; Zhao, L. Review Article: Inferring Permafrost and Permafrost Thaw in the Mountains of the Hindu Kush Himalaya Region. *Cryosphere* **2017**, *11*, 81–99. [[CrossRef](#)]
- Freitas, P.; Vieira, G.; Canário, J.; Folhas, D.; Vincent, W.F. Identification of a Threshold Minimum Area for Reflectance Retrieval from Thermokarst Lakes and Ponds Using Full-Pixel Data from Sentinel-2. *Remote Sens.* **2019**, *11*, 657. [[CrossRef](#)]
- Villarreal, C.D.; Tamburini Beliveau, G.; Forte, A.P.; Monserrat, O.; Morvillo, M. DInSAR for a Regional Inventory of Active Rock Glaciers in the Dry Andes Mountains of Argentina and Chile with Sentinel-1 Data. *Remote Sens.* **2018**, *10*, 1588. [[CrossRef](#)]
- Rucci, A.; Ferretti, A.; Monti Guarnieri, A.; Rocca, F. Sentinel 1 SAR Interferometry Applications: The Outlook for Sub Millimeter Measurements. *Sentin. Mission.-New Oppor. Sci.* **2012**, *120*, 156–163. [[CrossRef](#)]
- Gabriel, A.K.; Goldstein, R.M.; Zebker, H.A. Mapping Small Elevation Changes over Large Areas: Differential Radar Interferometry. *J. Geophys. Res. Solid Earth* **1989**, *94*, 9183–9191. [[CrossRef](#)]
- Massonnet, D.; Feigl, K.L. Radar Interferometry and Its Application to Changes in the Earth's Surface. *Rev. Geophys.* **1998**, *36*, 441–500. [[CrossRef](#)]
- Bürgmann, R.; Rosen, P.A.; Fielding, E.J. Synthetic Aperture Radar Interferometry to Measure Earth's Surface Topography and Its Deformation. *Annu. Rev. Earth Planet. Sci.* **2000**, *28*, 169–209. [[CrossRef](#)]

28. Ferretti, A.; Prati, C.; Rocca, F. Nonlinear Subsidence Rate Estimation Using Permanent Scatterers in Differential SAR Interferometry. *IEEE Trans. Geosci. Remote Sens.* **2000**, *38*, 2202–2212. [[CrossRef](#)]
29. Ferretti, A.; Prati, C.; Rocca, F. Permanent Scatterers in SAR Interferometry. *IEEE Trans. Geosci. Remote Sens.* **2001**, *39*, 8–20. [[CrossRef](#)]
30. Hooper, A.; Segall, P.; Zebker, H. Persistent Scatterer Interferometric Synthetic Aperture Radar for Crustal Deformation Analysis, with Application to Volcán Alcedo, Galápagos. *J. Geophys. Res. Solid Earth* **2007**, *112*, B07407. [[CrossRef](#)]
31. Cian, F.; Blasco, J.M.D.; Carrera, L. Sentinel-1 for Monitoring Land Subsidence of Coastal Cities in Africa Using PSInSAR: A Methodology Based on the Integration of SNAP and StaMPS. *Geosciences* **2019**, *9*, 124. [[CrossRef](#)]
32. Delgado Blasco, J.M.; Foumelis, M.; Stewart, C.; Hooper, A. Measuring Urban Subsidence in the Rome Metropolitan Area (Italy) with Sentinel-1 SNAP–StaMPS Persistent Scatterer Interferometry. *Remote Sens.* **2019**, *11*, 129. [[CrossRef](#)]
33. Foumelis, M.; Delgado Blasco, J.M.; Desnos, Y.-L.; Engdahl, M.; Fernandez, D.; Veci, L.; Lu, J.; Wong, C. Esa Snap—Stamps Integrated Processing for Sentinel-1 Persistent Scatterer Interferometry. In Proceedings of the IGARSS 2018—2018 IEEE International Geoscience and Remote Sensing Symposium, Valencia, Spain, 22–27 July 2018; pp. 1364–1367.
34. Mancini, F.; Grassi, F.; Cenni, N. A Workflow Based on SNAP–StaMPS Open-Source Tools and GNSS Data for PSI-Based Ground Deformation Using Dual-Orbit Sentinel-1 Data: Accuracy Assessment with Error Propagation Analysis. *Remote Sens.* **2021**, *13*, 753. [[CrossRef](#)]
35. Bekaert, D.P.S.; Hooper, A.; Wright, T.J. A Spatially Variable Power Law Tropospheric Correction Technique for InSAR Data. *J. Geophys. Res. Solid Earth* **2015**, *120*, 1345–1356. [[CrossRef](#)]
36. Foumelis, M. Vector-Based Approach for Combining Ascending and Descending Persistent Scatterers Interferometric Point Measurements. *Geocarto Int.* **2018**, *33*, 38–52. [[CrossRef](#)]
37. Riordan, B.; Verbyla, D.; McGuire, A.D. Shrinking Ponds in Subarctic Alaska Based on 1950–2002 Remotely Sensed Images. *J. Geophys. Res. Biogeosciences* **2006**, *111*, G04002. [[CrossRef](#)]
38. Smith, L.C.; Sheng, Y.; MacDonald, G.M.; Hinzman, L.D. Disappearing Arctic Lakes. *Science* **2005**, *308*, 1429. [[CrossRef](#)]
39. Sannel, A.B.K.; Kuhry, P. Warming-Induced Destabilization of Peat Plateau/Thermokarst Lake Complexes. *J. Geophys. Res. Biogeosciences* **2011**, *116*, G030035. [[CrossRef](#)]
40. Hassan, J.; Chen, X.; Muhammad, S.; Bazai, N.A. Rock Glacier Inventory, Permafrost Probability Distribution Modeling and Associated Hazards in the Hunza River Basin, Western Karakoram, Pakistan. *Sci. Total Environ.* **2021**, *782*, 146833. [[CrossRef](#)] [[PubMed](#)]
41. Schmid, M.-O.; Baral, P.; Gruber, S.; Shahi, S.; Shrestha, T.; Stumm, D.; Wester, P. Assessment of Permafrost Distribution Maps in the Hindu Kush Himalayan Region Using Rock Glaciers Mapped in Google Earth. *Cryosphere* **2015**, *9*, 2089–2099. [[CrossRef](#)]
42. Colombo, N.; Salerno, F.; Martin, M.; Malandrino, M.; Giardino, M.; Serra, E.; Godone, D.; Said-Pullicino, D.; Fratianni, S.; Paro, L.; et al. Influence of Permafrost, Rock and Ice Glaciers on Chemistry of High-Elevation Ponds (NW Italian Alps). *Sci. Total Environ.* **2019**, *685*, 886–901. [[CrossRef](#)] [[PubMed](#)]
43. Melis, M.T.; Pisani, L.; De Waele, J. On the Use of Tri-Stereo Pleiades Images for the Morphometric Measurement of Dolines in the Basaltic Plateau of Azrou (Middle Atlas, Morocco). *Remote Sens.* **2021**, *13*, 4087. [[CrossRef](#)]

Disclaimer/Publisher’s Note: The statements, opinions and data contained in all publications are solely those of the individual author(s) and contributor(s) and not of MDPI and/or the editor(s). MDPI and/or the editor(s) disclaim responsibility for any injury to people or property resulting from any ideas, methods, instructions or products referred to in the content.